CORONAL MASS EJECTION MASS, ENERGY, AND FORCE ESTIMATES USING *STEREO*

Eoin P. Carley [1], R. T. James McAteer [2], and Peter T. Gallagher [1]
Draft version April 23, 2012

ABSTRACT

Understanding coronal mass ejection (CME) energetics and dynamics has been a long-standing problem, and although previous observational estimates have been made, such studies have been hindered by large uncertainties in CME mass. Here, the two vantage points of the *Solar Terrestrial Relations Observatory (STEREO)* COR1 and COR2 coronagraphs were used to accurately estimate the mass of the 2008 December 12 CME. Acceleration estimates derived from the position of the CME front in 3-D were combined with the mass estimates to calculate the magnitude of the kinetic energy and driving force at different stages of the CME evolution. The CME asymptotically approaches a mass of $3.4 \pm 1.0 \times 10^{15}$ g beyond $\sim 10\,R_\odot$. The kinetic energy shows an initial rise towards $6.3 \pm 3.7 \times 10^{29}$ erg at $\sim 3\,R_\odot$, beyond which it rises steadily to $4.2 \pm 2.5 \times 10^{30}$ erg at $\sim 18\,R_\odot$. The dynamics are described by an early phase of strong acceleration, dominated by a force of peak magnitude of $3.4 \pm 2.2 \times 10^{14}$ N at $\sim 3\,R_\odot$, after which a force of $3.8 \pm 5.4 \times 10^{13}$ N takes affect between ~ 7–$18\,R_\odot$. These results are consistent with magnetic (Lorentz) forces acting at heliocentric distances of $\lesssim 7\,R_\odot$, while solar wind drag forces dominate at larger distances ($\gtrsim 7\,R_\odot$).

Subject headings: Sun: corona – Sun: coronal mass ejections (CMEs)

1. INTRODUCTION

Despite many years of study, the origin of the forces that drive coronal mass ejections (CMEs) in the solar corona and interplanetary space are not well understood. From an observational viewpoint a complete understanding of CME kinematics, dynamics and forces requires not only a study of CME speed, acceleration and expansion but also an accurate knowledge of CME mass. The measurements of CME mass combined with acceleration measurements can be used to quantify the magnitude of the force that drives a CME. Knowledge of this force magnitude can lead to an identification of the possible origin of the CME driver.

There are numerous theoretical models that attempt to explain the triggering of CME eruption and its consequent propagation. Each describe the destabilization and propagation of a complex magnetic structure, such as a flux rope, via mechanisms that include the catastrophe model (Forbes & Isenberg 1991; Forbes & Priest 1995; Lin & Forbes 2000), magnetic breakout model (Antiochos et al. 1999; Lynch et al. 2008), or a toroidal instability model (Chen 1996; Kliem & Török 2006). The loss of equilibrium induced by such mechanisms results in CME propagation into interplanetary space. The predictions of these models have been investigated in observational studies whereby the CME kinematics are used to constrain what forces might be at play and hence which model best describes CME propagation. Such studies show that early phase propagation can be reasonably described by the existing models (or a combination of them) involving some form of magnetic CME driver (Manoharan & Kundu 2003; Chen et al. 2006; Schrijver et al. 2008; Lin et al. 2010), and that aerodynamic drag of the solar wind may have a significant role at later stages of

CME propagation (Howard et al. 2007; Maloney & Gallagher 2010; Byrne et al. 2010). Comparisons between modeling and observational estimates of the forces that drive CMEs requires an accurate determination of CME kinematics properties as well as CME mass.

To date, the most prevalent method of determining CME mass has been through the use of white light coronagraph imagers, such as the Large Angle Spectroscopic Coronagraph (LASCO; Brueckner et al. 1995) on board the *Solar and Heliospheric Observatory* (*SOHO*; Domingo et al. 1995) and the twin Sun Earth Connection Coronal and Heliospheric Investigation (SECCHI) COR1 and COR2 coronagraphs (Howard et al. 2008) on board the *Solar Terrestrial Relations Observatory* (*STEREO*; Kaiser et al. 2008). The white-light emission imaged by such coronagraphs occurs via Thomson scattering of photospheric light by coronal electrons (Minnaert 1930; van de Hulst 1950; Billings 1966), the so called K-corona. From classical Thomson scattering theory, the intensity of the light detected by an observer depends on the particle density of the scattering plasma. Hence, any density enhancement, such as a CME, over the background coronal density appears as enhanced emission in white light. The enhanced emission allows for a calculation of the total electron content and hence mass.

Some of the first measurement of CME mass using scattering theory were carried out by Munro et al. (1979) and Poland et al. (1981) using space-based white light coronagraphs on board *SkyLab* and U.S. military satellite *P78-1*. Both the early studies and later statistical investigations determined that the majority of CMEs have masses in the range of 10^{13}–10^{16} g, (Vourlidas et al. 2002, 2010). However, due to only a single viewpoint of observation, the longitudinal angle at which the CME propagates outwards was largely unknown in these studies and it is generally assumed that the CME propagates perpendicular to the observers line-of-sight (LOS). There is also the added assumption that all CME mass lies in the two-

[1] Astrophysics Research Group, School of Physics, Trinity College Dublin, Dublin 2, Ireland.
[2] Department of Astronomy, New Mexico State University, Las Cruces, New Mexico 88003-8001, USA.

dimensional plane-of-sky (POS). Such assumptions can lead to a mass underestimation of up to 50% or more (Vourlidas et al. 2000). More recent studies have employed the two viewpoint capabilities of the *STEREO* mission to determine the mass of numerous CMEs with much less uncertainty (Colaninno & Vourlidas 2009).

In this paper, we analyze mass development of the 2008 December 12 CME using the *STEREO* COR1 and COR2 coronagraphs.We use a well constrained angle of propagation to determine the mass and position of the CME. Combining the mass measurements with values for CME velocity and acceleration, the kinetic energy and the magnitude of the force influencing propagation is determined for each point in time. Section 2 describes the observations of the event from first appearance of the front in COR1 A and B to the time when the front exits the COR2 A and B fields of view. Section 3 describes the methods by which the mass, energy, and force are calculated with *a priori* knowledge of the propagation angle. Section 4 includes the results and Section 5 discusses the possible forces attributable to the observed accelerations and whether they are magnetic or aerodynamic in origin. This is followed by conclusions in Section 6.

2. OBSERVATIONS

The COR1 images used in this analysis span from 2008 December 12 04:05 UT to 15:45 UT, with a cadence of 10 minutes. The three polarization states of COR1 were combined to make total brightness images in units of mean solar brightness (MSB). Base difference images were produced using the 04:05 UT image (in both COR1 A and B) as a background to be subtracted from all subsequent images. A sample of such images for both COR1 A and B can be found in Figure 1. The COR2 images analyzed range from from 07:22 UT to 17:52 UT, with a cadence of 30 minutes. As with the COR1 images, total brightness images were created for COR2, and a set of base difference images were then produced using the 07:22 UT image as a suitable background. A selected set of images from COR2 can be found in Figure 2.

At 04:35 UT the leading edge of a CME appeared in COR1 A and B coronagraphs at a height of $\sim 1.4\,R_\odot$, off the east and west limb respectively. In COR1 B the CME first appears as a set of rising loop-like structures followed by a prominence, part of which appears to fall back to the surface at 08:00 UT while the remainder was ejected and follows the rising loop-like structures which eventually become the CME front. The rising prominence was not apparent at any stage of the propagation in COR1 A and the advancing front remains the only distinguishable facet of the CME from this line-of-sight (LOS).

A noteworthy caveat of using base difference imaging is the assumption that the background corona in the pre-event image has the same brightness in all subsequent images. This may not always be true and any excess brightness in the pre-event image will produce negative pixel values in the base difference. This is apparent in the COR1 images as the CME interacts with a streamer, displacing it as the leading CME front expands laterally as well as moves outward. The streamer is visible as a dark feature that grows with time at the southward flank of the CME in the COR1 B images, Figure 1. The black areas are indicative of negative pixel values. The COR1 A images also suffer from negative pixels, especially at later

times, see Figure 1 top row, 09:15 UT image. The front of the CME starts to exit both the A and B field of view at $\sim 08:35$ UT.

The CME first appears in the COR2 field of view at $\sim 07:52$ UT with the CME apex at a height of $\sim 3\,R_\odot$ in both A and B images. In the B coronagraph, by 10:52 UT the three part structure of core, cavity, and bright front is clearly visible and the overall structure grows in size as the CME propagates to larger heights. The core becomes more tenuous and the mass distribution becomes homogenous after 15:52 UT when the front starts to exit the field of view. The distinction between core and front is not as clear in COR2 A and the mass distribution appears more homogenous throughout the propagation. As with the COR1 images, COR2 A is also affected by excess brightness in the pre-event image, as is apparent by a growing dark feature in its southern half. As the pre-event image for COR2 B is the cleanest of the pre-event images (it contains the least contamination by streamers), the COR2 B data are considered the best candidate for accurate CME mass measurements.

3. CME MASS MEASUREMENT METHODS

The method by which mass measurements are derived from white light coronagraph images is based on theory first developed by Minnaert (1930) in which the scattering geometry of a single electron at a particular point in the solar atmosphere is considered. Further development of the theory by van de Hulst (1950) led to the derivation of what are now known as the van de Hulst coefficients. The coefficients treat each component of the incident electric field vector separately and take into account the finite size of the solar disk (Minnaert 1930; Billings 1966; Howard & Tappin 2009). An important fact arising from these expressions is the dependence of scattering intensity on the angle, χ, between the radial vector from sun centre to the scattering electron and a position vector from observer towards the electron–the LOS, see Figure 3. Scattering efficiency is minimized when this angle is 90°. However, along the LOS such an angle occurs at the point of minimum distance from sun centre where the incident intensity (that the electron receives) and electron density are maximized. This means scattered light in the corona is most intense along a plane perpendicular to the observer's LOS despite the efficiency of scattering being minimized at such viewing angles (Howard & Tappin 2009). This plane perpendicular to the LOS is known as the plane-of-sky (POS)

Studies using single LOS coronagraph data are often hindered by the unknown CME propagation angle from the POS, e.g., unknown θ (or χ) in Figure 3. This leads to the incorrect angle being used when inverting the van de Hulst coefficients to calculate the number of electrons contributing to the scattered light. Furthermore, because the 3-D extent of the CME is unknown it is also assumed that the CME is confined to the 2-D sky plane, leading to a significant CME mass underestimation (Vourlidas et al. 2000).

The CME of 2008 December 12 was Earth-directed (Byrne et al. 2010), making it roughly the same angular distance from both the *STEREO* A and B spacecraft, then located ±45 degrees from Earth. This known angle of propagation was used to convert from pixel values of
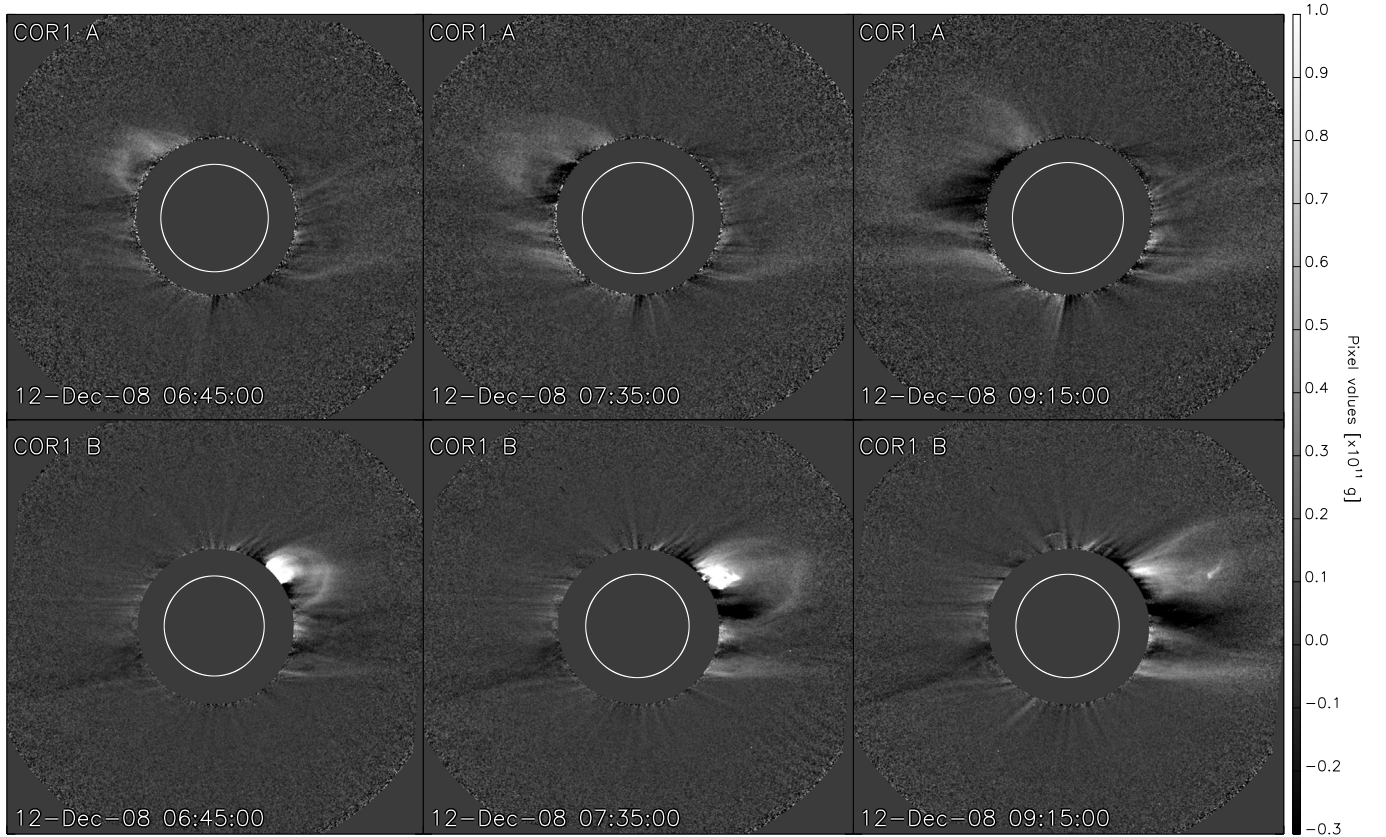
FIG. 1.— Selection of base difference images of the CME in COR1 A (top row) and COR1 B (bottom row), with pixel values of grams. The CME is quite faint in the A images and appears not to have as much structure as in B. There is a large contribution to mass from a near-saturated region to the upper flank of the CME in the B images. Such saturation in the mass images coincides spatially with the prominence in total brightness images.

MSB to grams via the expression

$$m_{pixel} = \frac{B_{obs}}{B_e} \times 1.97 \times 10^{-24}\,\text{g} \qquad (1)$$

where B_{obs} is the observed MSB of the pixel, B_e is the electron brightness calculated from the van de Hulst coefficients, and 1.97×10^{-24} g is a factor that converts the number of electrons to mass, assuming a completely ionized corona with a composition of 90% hydrogen and 10% helium. The known angle of propagation allowed the correct value of B_e to be computed resulting in a significant reduction in the uncertainties associated with the propagation angle. The largest remaining uncertainty is the unknown angular width along the LOS. This uncertainty was quantified in a similar approach to the method outlined in Vourlidas et al. (2000). This simulates the brightness of a CME with homogeneous density distribution and finite angular width along the LOS–longitudinal angular width $\Delta\theta_{long}$, allowing calculation of a simulated observed mass. Comparing this to the actual mass allowed for an evaluation of CME mass underestimation for given values of $\Delta\theta_{long}$. Since the values for $\Delta\theta_{long}$ are unknown, the expression derived in Byrne et al. (2010) for the *latitudinal* angular width of this CME as a function of height, $\Delta\theta_{lat}(r) = 25r^{0.22}$, was used to define an upper limit to $\Delta\theta_{long}$. It was assumed the CME longitudinal angular width is no more than twice the latitudinal angular width, or $\Delta\theta_{long} \leqslant 2 \times \Delta\theta_{lat}$. Such an upper limit is in agreement with simulations of flux-rope CMEs

which give a typical aspect ratio of broadside to axial angular extents of $1.6-1.9$ (Krall & St. Cyr 2006). Hence the value for $\Delta\theta_{long}$ at each height was used to obtain the simulated mass underestimation estimates described above. The heights and angular widths used in this study produced CME mass underestimation estimates of between 5–10% for finite angular width uncertainty. An extra mass uncertainty of 6% was added to account for the assumption of coronal abundance of 90% hydrogen and 10% helium which can lead to slight errors while converting from pixel values of MSB to grams (Vourlidas et al. 2010).

To calculate the CME mass a user-selected area (the extent of the CME, for example) of the base difference image was chosen and the pixel values within this area were summed to obtain total mass. Figure 2 COR2 B images show an example of the sector over which pixels were summed (the smaller sectors indicate a different summing region used at a later stage). The selected area was chosen for each image in the time sequence of CME propagation so as to determine the mass variation with height in COR1 and 2 using both A and B. The selection of an area by a point and click method is of course a subjective identification of the the extent of the CME, so it is susceptible to user-generated uncertainties. To quantify these uncertainties the mass was obtained for each coronagraph image in the time sequence (as described above) and the process was repeated five times in order to obtain the mean CME mass for each image and the
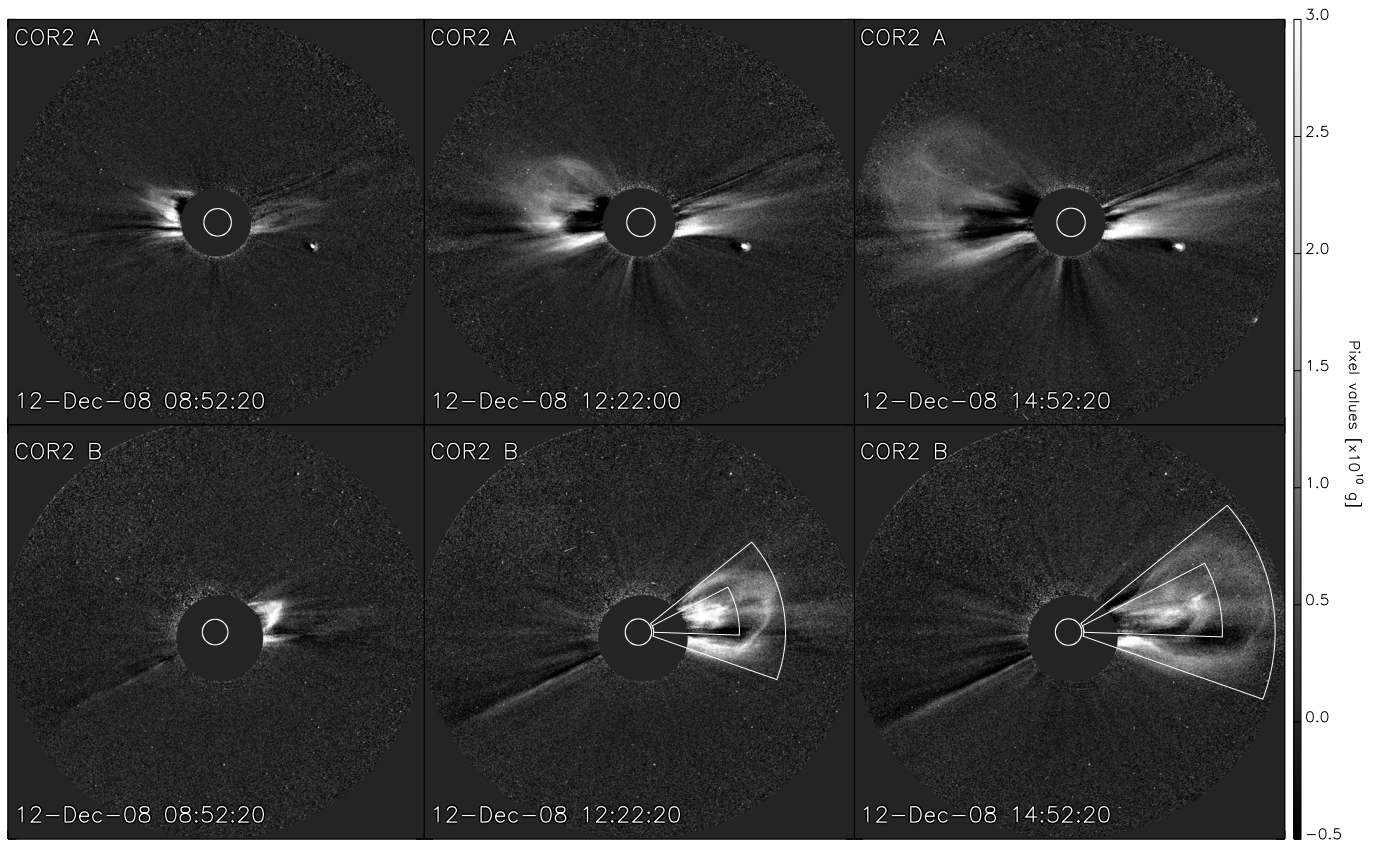
FIG. 2.— Selection of base difference images of the CME in COR2 A (top row) and COR2 B (bottom row), with pixel values of grams. The CME is clearly distinguishable in both fields of view. Only the B field view shows clearly the three part structure of core, cavity and front. The COR2 B images were used to measure core and front mass separately
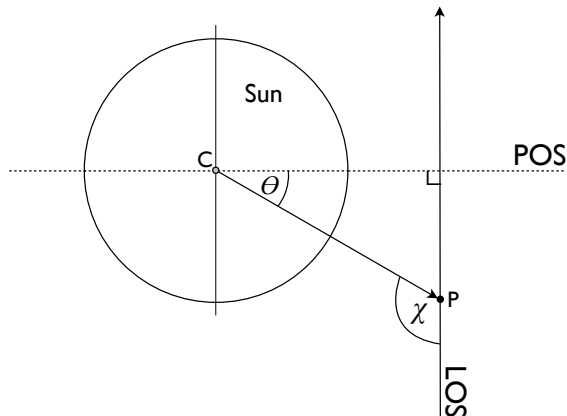

FIG. 3.— Schematic showing the relative orientation of the line-of-sight (LOS), and the plane-of-sky (POS). Electron position is at point P and C is Sun center. The vector CP may also represent CME propagation direction. Scattering efficiency is heavily dependent on the angle θ (or χ) and is least efficient when $\theta = 0°$ ($\chi = 90°$).

standard error on the mean. This standard error was defined as the uncertainty due to user bias in the point and click method of CME identification. The height at each measurement interval was taken to be the heliocentric distance of the CME apex in the image i.e., the apex of the front was chosen by simple point-and-click method. The uncertainty on the apex height was also found by the standard error on five runs.

The deflection of a small streamer during CME propagation produces negative pixels in the base difference images. The effect is particularly apparent in the COR1 images, Figure 1. It is difficult to unambiguously distinguish between streamer and CME, making it difficult to quantify the uncertainty introduced due to streamer interaction. To make an estimate of the streamer's effects, a calculation of its mass in the pre-event image was made. A number of different samples of the area of the streamer in the COR1 B pre-event image that effects all subsequent images produced a mass estimate of $\sim 5 \times 10^{14}$ g. This mass was used as a measure of the uncertainty introduced due to streamer interaction in the COR1 B images. A similar analysis of the COR1 A pre-event images gave a streamer mass estimate of $\sim 7 \times 10^{14}$ g. COR2 images are relatively unaffected by significant changes in background coronal brightness and do not suffer from negative pixel values to as large an extent as COR1. The pre-event image of COR2 B is particularly clean and free of background streamers, hence COR2 B images are considered to provide most accurate CME mass estimation.

Finally, in order to obtain a more complete and continuous estimate of CME mass growth, the masses determined from both COR1 and COR2 coronagraphs were summed in those cases where image times of the inner and outer coronagraphs overlapped[3]. The overlap in the

[3] A difference in cadence of the inner and outer coronagraphs means that the images closest in time have a three minute offset e.g., a COR1 image taken at 07:25 UT was considered to be coincident in time with the COR2 image at 07:22 UT

inner and outer corongraphs' fields of view was also taken into account in this summation.

A concise measurement of the CME kinematics, such as velocity and acceleration, were taken from the results of the study of Byrne et al. (2010). Since these kinematics take into account the true three dimensional surface of the front they provide reliable estimates of CME velocity and acceleration in 3-D space. These velocity and acceleration measurements were used in the calculation of kinetic energy and total force on the CME for each point in time. The CME mass used in all energy and force calculations was the asymptotic mass it approaches at later stages of its evolution beyond $10\,R_\odot$ as observed from the *STEREO B* spacecraft i.e., $3.4\pm1.0\times10^{15}$ g. As will be shown, there is good motivation for the use of constant mass in the magnitude of kinetic energy and force estimates.

4. RESULTS

4.1. *CME Mass Estimates*

The results of the calculation for CME mass development with time and height for both *STEREO* A and B coronagraphs are shown in Figure 4. In panel (a), the height values are those taken from a point-and-click method of tracking the CME apex; these heights are corrected for CME propagation angle of $\sim45°$. In both panels (a) and (b), the mass estimates of *STEREO* A and B follow a similar trend and have similar values at each stage in the propagation. Such good agreement between mass values is a good indicator that $\sim45°$ is the correct angle of propagation from the sky-plane. A change in the cadence of mass measurements is noticeable at $\sim08{:}00$ UT (or $\gtrsim5\,R_\odot$). This is due to the use of only COR1 images (with a cadence of 10 minutes) prior to this time, and the use of the COR2 plus COR1 images after this time (the cadence of these measurements follows that of COR2 – 30 minutes). Comparing A and B below $4.5\,R_\odot$, mass values show a similar trend and increase at the same rate, but at approximately $3\,R_\odot$ the mass measurements in COR1 B appear to increase to a much larger value then fall again. This effect is visible in the COR1 A measurements, albeit diminished. It is probably due to the presence of a prominence which contains a significant mass content and therefore contributes a large amount to total measured CME mass. Also, early on in its propagation, the prominence may still be emitting H-α line radiation (656.28 nm) due to the larger fraction of neutral hydrogen at its cooler temperatures. The COR1 imaging passband is centered on H-α so any emission in the prominence from neutral hydrogen could be contributing to light received by the COR1 coronagraphs, this is apparent from the saturation region in the COR1 B images in Figure 1. Since this is resonance line emission, and not Thomson scattered emission, it leads to an erroneous measurement in CME mass. Thus, it is assumed the larger rise and fall in CME mass is caused by the prominence entering and exiting the COR1 B field of view. The effect is diminished in COR1 A since the prominence does not enter the FOV to as large an extent as in COR1 B. The interpretation that the 'mass bump' is not actual mass growth (or loss) is supported by previous measurements where CME mass increase follows a trend with height described by $M_{cme}(h) = M_a(1 - e^{-h/h_a})$, where
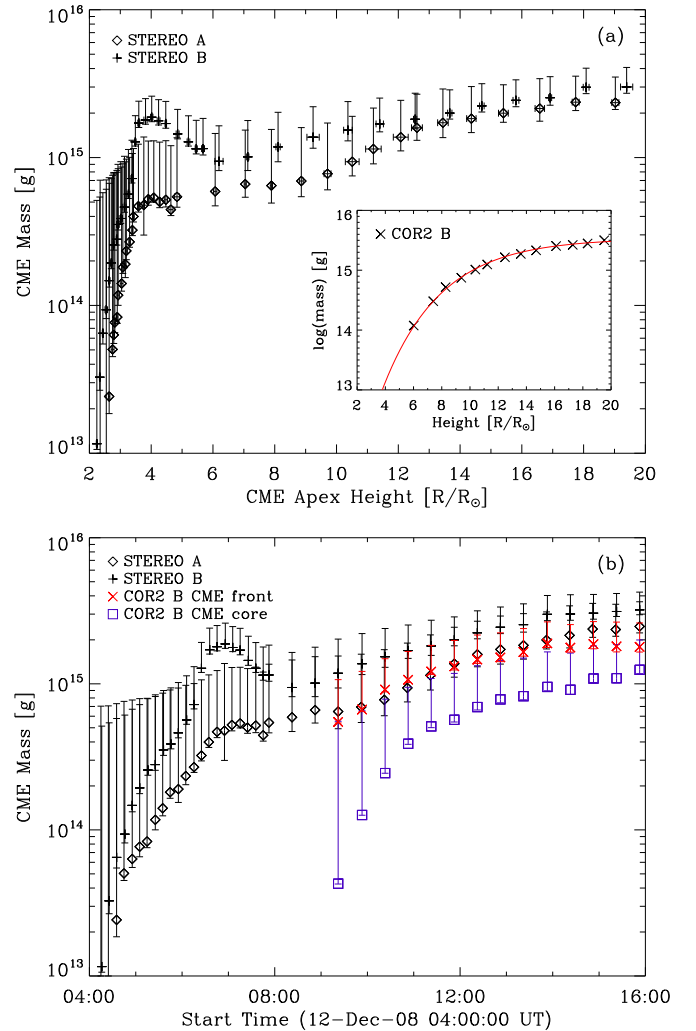

FIG. 4.— CME mass development with height (a) and time (b), for the 2008 December 12 CME. After $\sim08{:}00$ UT ($\gtrsim5\,R_\odot$) the masses from the inner and outer coronagraphs are summed to show uninterrupted mass development from ~2–$20\,R_\odot$ over a period of 12 hours. The small bump in the CME mass at $\sim07{:}00$ UT ($\sim4\,R_\odot$) is probably due to an unknown amount of H-α emission from the prominence. Mass of CME front and core are also shown, red '×' and blue square, for COR2 B, panel (b). After 14:52 UT they share approximately equal mass. The inset of (a) shows mass development with height for COR2 B only; the red curve represents a fit to the data whereby the mass asymptotically approaches $3.4\pm1.0\times10^{15}$ g.

M_a is the final mass the CME approaches asymptotically and h_a is the height at which the CME reaches $0.63M_a$ (Colaninno & Vourlidas 2009), with no 'bump' in mass earlier on. The decline in mass after the peak may be explained by the ionization of neutral hydrogen such that H-α emission diminishes and simply becomes Thomson scattering of free electrons, as with the rest of the CME material.

In order to produce a fit to the data, the COR2 B mass results were chosen because its pre-event image was largely free of any bright streamers or other features which introduce unwanted effects in the production of base difference images, as described above. A fit with the above equation resulted in a final asymptotic CME mass of $3.4\pm1.0\times10^{15}$ g, with a scale height of $h_a = 2.9\,R_\odot$. This fit is plotted along with the COR2 B data in the in-

set panel of Figure 4(a). Note that the mass increase is due to material coming up from below the occulting disk, and not actual mass gain of the CME. The uncertainty on the above asymptotic mass value was taken to be 30%, from the largest uncertainty due to finite width, the conversion factor uncertainty as described above, the standard error user-generated uncertainty, and uncertainty due to streamer interaction.

In each image where the CME core and front are distinguishable, their masses were measured separately. This was carried out by user selected regions demarcating the areas of core and front, see COR2 B at 12:22 UT and 14:52 UT in Figure 2 for an example of the separate core and front sectors over which pixel values were summed to obtain total mass. The uncertainties due to finite width of the observed object also apply to the core and front measurements, however, since the widths of these particular areas of the CME are unknown we chose the maximum uncertainty of 10% from the above analysis since neither core nor front can be any wider than the maximum width assigned to this CME. The remaining uncertainties described above were also applied. The mass development of core and front with time is shown in Figure 4(b). The two mass measurements are subject to an observational effect of apparent exponential mass growth, however by the time the CME is fully in the field of view at 14:45 UT the core and front share approximately equal mass.

4.2. CME Forces and Energetics

In the following calculations, all measurements of force and kinetic energy use the asymptotic mass of $3.4 \pm 1.0 \times 10^{15}$ g and not the instantaneous mass values calculated from each coronagraph image i.e., the CME is considered to begin its propagation with this mass and does not acquire any mass as it propagates.

Estimates of the force and kinetic energy use the 3-D velocity and acceleration measurements produced by Byrne et al. (2010). Their method firstly identifies the CME front in each coronagraph image using a multiscale edge detection filter. The front edges were then used to define a quadrilateral in space into which an ellipse is fit, this method is known as elliptical tie-pointing. This was done for multiple horizontal planes through the CME so that the fit ellipses outline a curved front in 3-D space. The speed and acceleration were then deduced from the change in position of the front, with time, through the *STEREO* COR1, COR2 and HI fields of view. Since mass measurements in this study use only the COR1 and COR2 coronagraphs, HI kinematics measurements have been excluded here. The CME front position uncertainty in *STEREO A* and *B* coronagraphs was determined from the filter width in the multiscale analysis. Velocity and acceleration uncertainties were then propagated from position uncertainty. Figure 5(a) shows CME velocity as a function of heliocentric distance, along with acceleration in panel (b).

The CME kinetic energy was calculated using $E_{kin} = 1/2 M_{cme} v_{cme}^2$, where M_{cme} is the final asymptotic mass of $3.4 \pm 1.0 \times 10^{15}$ g and v_{cme} are the instantaneous velocity measurements, results of this calculation are shown in Figure 5(c). The kinetic energy shows an initial rise towards $6.3 \pm 3.7 \times 10^{29}$ ergs at $\sim 3 R_{\odot}$, beyond which it
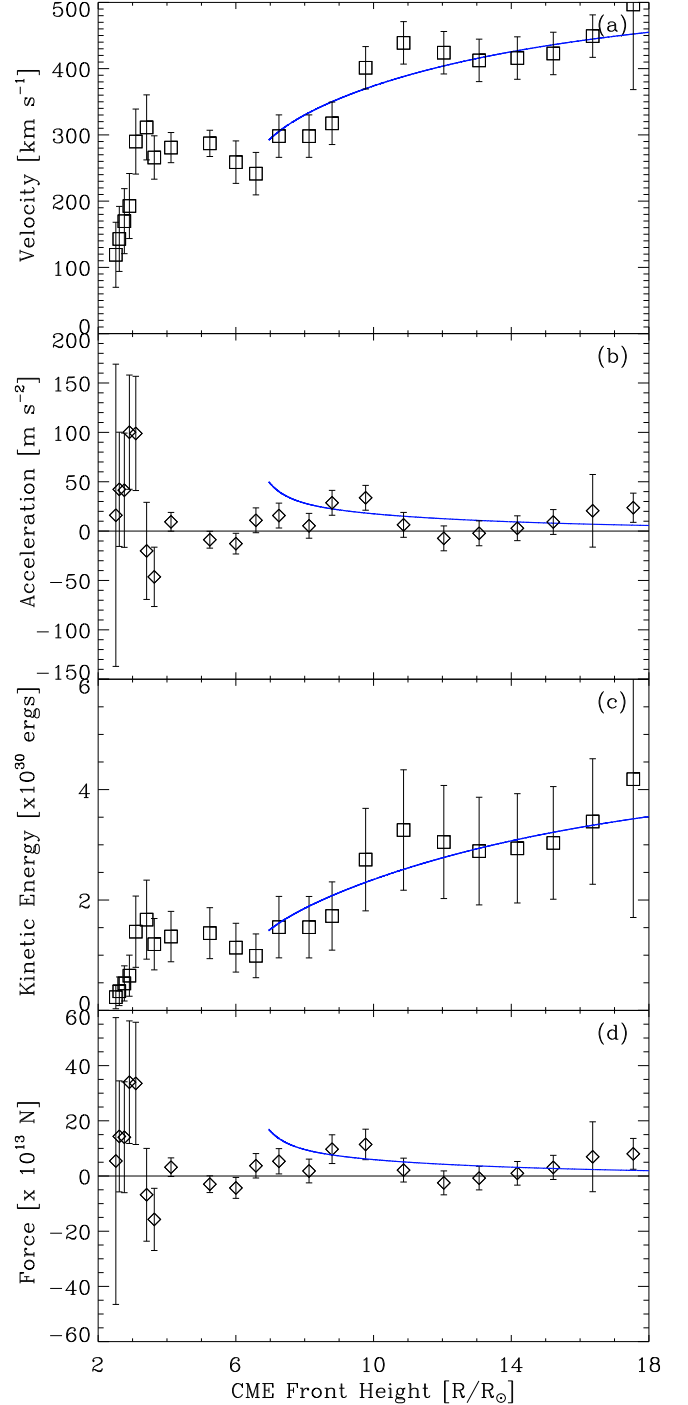

FIG. 5.— (a) CME velocity as a function of heliocentric distance, including a fit to the data produced using an aerodynamic drag model beyond $\sim 7 R_{\odot}$ (Byrne et al. 2010). (b) Acceleration of CME, including fit, derived from the velocity data and fit. Panel (c) and (d) show the kinetic energy and force, respectively, both calculated using constant CME mass of $3.4 \pm 1.0 \times 10^{15}$ g and kinematics results from (a) and (b). Also shown are the fits to energy and force produced from fits to velocity and acceleration.

rises steadily to $4.2 \pm 2.5 \times 10^{30}$ ergs at $\sim 18 R_{\odot}$, these values are similar to those reported in Vourlidas et al. (2000, 2010) and Emslie et al. (2004).

The total force on the CME was calculated using $F_{total} = M_{cme} a_{cme}$, where M_{cme} is as above and

a_{cme} is taken from the instantaneous acceleration values. As shown in panel (d) of Figure 5, the force initially grows significantly, reaching a maximum value of $3.4 \pm 2.2 \times 10^{14}$ N at $\sim 3\,R_\odot$. The early rise and fall in acceleration (or force) is in agreement with a previous study of a CME observed to reach peak acceleration at $\sim 1.7\,R_\odot$ after which it reaches a constant velocity beyond $\sim 3.4\,R_\odot$ (Gallagher et al. 2003). Such results are also found in a statistical study which shows that the majority of CMEs have peak acceleration in the low corona with a mean height of maximum acceleration at $1.5\,R_\odot$ (Bein et al. 2011). Similarly, observational studies by Zhang et al. (2001) and Zhang et al. (2004) also show early phase peak acceleration between 2–$5\,R_\odot$ and forces on the order of 10^{15} N and 10^{12} N, depending on whether the CME shows large initial acceleration or a slow, more gradual acceleration.

After this early peak, the force drops to an average value of $3.8 \pm 5.4 \times 10^{13}$ N at distances between 7–$18\,R_\odot$. It is apparent from Figure 5(a) that the velocity continues to increase beyond $7\,R_\odot$, implying that a positive radial force must be present. To clarify this, a fit to the velocity data using a model for solar wind drag on the CME beyond $7\,R_\odot$ (as outlined in Byrne et al. (2010)) is shown in Figure 5(a). Although the data suggest a non-monotonic increase in velocity, the fit reveals that propagation is best described by a steadily increasing velocity between 7–$18\,R_\odot$. The acceleration and kinetic energy curves derived from this velocity fit are shown in Figure 5(b) and (c). In Figure 5(d), the curve for the force derived from the velocity fit initially deviates from the data at $\sim 7\,R_\odot$, however beyond this distance there is good agreement with the data and the derived force is entirely positive. This suggests that the solar wind exerts a positive aerodynamic drag force on the CME, resulting in a velocity that approaches the asymptotic solar wind speed at large heliospheric distances.

5. DISCUSSION

It should be noted that Figure 4 shows an overall exponential increase in CME mass with height which could be interpreted as the CME rapidly gaining mass as it propagates. Care should be taken with this interpretation since this apparent exponential mass increase is almost certainly due to the CME moving into the field of view, therefore allowing us to measure more of its mass content; such an interpretation is in agreement with similar assertions made in Vourlidas et al. (2010). It is difficult to distinguish between actual CME mass growth and an apparent growth due to more of the CME being observed. If the initial early rise in CME mass is assumed to be an observational artifact then we can interpret the CME mass to be in the range of $(3$–$3.5) \times 10^{15}$ g for most of its early propagation i.e., the CME already has such a mass before launch and does not acquire more mass (via inflows or otherwise) during propagation. Such an interpretation is in agreement with CME mass measurements calculated from dimmings in *STEREO* Extreme Ultraviolet Image (EUVI) images, which show the mass calculated from EUV images to be approximately equal to CME mass in COR2 images, $m_{EUVI}/m_{COR2} = 1.1 \pm 0.3$ (Aschwanden et al. 2009). Once the CME bubble is in the field of view at $\sim 10\,R_\odot$ the mass in its entirety can be measured and the increase beyond this point, if any,

is slow and steady, Figure 4.

The early stages of CME propagation are dominated by a sharp rise to a peak force of $3.4 \pm 2.2 \times 10^{14}$ N at $\sim 3\,R_\odot$ followed by a sharp decline, Figure 5(d). The catastrophe model (Forbes & Isenberg 1991; Forbes & Priest 1995; Lin & Forbes 2000), magnetic breakout model (Antiochos et al. 1999; Lynch et al. 2008), and toroidal instability model (Chen 1996; Kliem & Török 2006) employ a number of forces acting on the CME to produce an over all acceleration into interplanetary space. For example, the toroidal instability model used by Chen (1996) uses a Lorentz hoop force (or Lorentz self-force), solar wind drag, and gravity to provide a net force acting on the CME between 2–$3\,R_\odot$ that quickly rises to a peak total force of $\sim 10^{16}$ N and then falls rapidly.

If we assume that the peak force observed for the 2008 December 12 CME is the net force due to similar forces used in the above models, such as the solar wind drag, gravity, and some form of magnetic CME driver e.g., a $\vec{J} \times \vec{B}$ force, we may estimate their relative contribution. The force due to solar wind drag on the CME is given by

$$\vec{F}_d = -\frac{1}{2} C_d \rho_{sw} A_{cme} (\vec{v} - \vec{v}_{sw}) \mid \vec{v} - \vec{v}_{sw} \mid \qquad (2)$$

where M_{cme} is the CME mass, $\vec{v}$ is the CME velocity, C_d is the drag coefficient, ρ_{sw} is the solar wind mass density, A_{cme} is the CME area exposed to solar wind drag and $\vec{v}_{sw}$ is the solar wind velocity (Maloney & Gallagher 2010). To estimate the effects of this force we use $\rho_{sw} = n_p m_p$, where m_p is proton mass, and assume ionization fraction of $\chi = 1$ such that $n_p = n_e\,[cm^{-3}]$. Electron density, and hence proton density, is then given by an interplanetary density model derived from a special solution of the Parker solar wind equation (Mann et al. 1999), solar wind velocity values as a function of height are also determined using this model. A_{cme} is estimated using the expression derived in Byrne et al. (2010) for latitudinal angular width of the CME as a function of height, $\Delta\theta_{lat}(r) = 26r^{0.22}$. This is used to derive an arc length of the CME front and, as above, making the assumption $\Delta\theta_{long} = 2 \times \Delta\theta_{lat}$, the two arc lengths derived from these angles then give the surface that the solar wind acts on, thus $A_{cme} = 1352r^{2.44}$. Setting the drag coefficient $C_d = 1$, and using the Mann et al. (1999) model to derive a density and a solar wind velocity of 2.3×10^5 cm^{-3} and $70\,\mathrm{km\,s^{-1}}$, respectively, equation [1] then gives a force of $\vec{F}_d = -8.0 \times 10^{12}\,\hat{r}$ N for solar wind drag at $\sim 3\,R_\odot$, where $\hat{r}$ is a unit vector in the positive radial direction.

A simple estimate of force due to gravity is given by $\vec{F}_g = GM_\odot M_{cme}/\vec{r}^{\,2}$, where G is the universal gravitational constant, $M_\odot$ is solar mass, M_{cme} is CME mass, and $\vec{r}$ is a heliocentric position vector[4]. Given a CME mass of 3.4×10^{15} g the force due to gravity at a heliocentric distance of $3\,R_\odot$ is $\vec{F}_g = -1.0 \times 10^{14}\,\hat{r}$ N. The only remaining contribution is due to some form of magnetic

---

[4] Ideally the heliocentric distance of the CME centre of mass would be used here. However an unknown amount of mass is obscured by the coronagraphs occulting disk, making the mass distribution and hence COM difficult to determine. Thus the CME front height is used in the calculation of force due to gravity

CME driver, F_{mag}, which is estimated using

$$\vec{F}_{mag} = \vec{F}_{total} - \vec{F}_d - \vec{F}_g \qquad (3)$$

(the pressure gradient in the CME equation of motion is assumed to be negligable and has been omitted here). Using the above values, the total magnetic contribution to CME force is calculated to be $\vec{F}_{mag} \approx 4.5 \times 10^{14} \, \hat{r}$ N at $3\,R_\odot$, indicating that this is the largest driver of CMEs at low coronal heights. Lorentz force dominated dynamics in early phase CME propagation are reported in Bein et al. (2011), in which a statistical study of a large sample of CMEs in EUVI, COR1, and COR2 indicated an early phase acceleration for the majority of CMEs that is attributable to a Lorentz force. A similar result of an observational study by Vršnak (2006) found that the Lorentz force plays a dominant role within a few solar radii. It should be noted that although we have labelled the force F_{mag}, there is no distinction on the exact form of this force e.g., whether it is magnetic pressure, magnetic tension, or a Lorentz self-force that acts as the driver. Also, any non-radial motion of the CME, such as that described in Byrne et al. (2010), is not taken into account here; any force estimates are purely radial in direction.

6. CONCLUSION

The *STEREO* COR1/2 coronagraphs have been used to determine the mass development of the 2008 December 12 CME. Knowledge of the longitudinal propagation angle of the CME allowed for a significant reduction in the mass uncertainty, giving a final estimate of $3.4 \pm 1.0 \times 10^{15}$ g. Using kinematics results of a previous study (Byrne et al. 2010), the velocity and acceleration of the CME were combined with the mass measurements

to determine the kinetic energy and total force on the CME. The early phase propagation of the CME was found to be dominated by a force of peak magnitude of $3.4 \pm 2.2 \times 10^{14}$ N at $\sim 3.0\,R_\odot$, after which the magnitude declines rapidly and settles to and average of $3.8 \pm 5.4 \times 10^{13}$ N. This early rise and fall in total force (or acceleration) is in agreement with previous observations of CME kinematics (Gallagher et al. 2003; Bein et al. 2011). Similarly results of observational studies by Zhang et al. (2001) and Zhang et al. (2004) also show early phase peak acceleration between 2–$5\,R_\odot$ and forces on the order of 10^{15} N and 10^{12} N. The kinetic energy shows an initial rise towards $6.3 \pm 3.7 \times 10^{29}$ ergs at $\sim 3\,R_\odot$, beyond which it rises steadily to $4.2 \pm 2.5 \times 10^{30}$ ergs at $\sim 18\,R_\odot$, such order of magnitudes are similar to those reported in Vourlidas et al. (2000); Emslie et al. (2004) and are typical of CME kinetic energies (Vourlidas et al. 2010).

Such CME kinematics and dynamics property estimates cannot be carried out when unknown propagation angle hinders an accurate calculation of CME mass, hence adding unacceptable uncertainty to any subsequent calculations. This highlights the need for similar studies using the *STEREO* mission's ability to accurately determine the physical properties of CMEs, such as mass, with remarkably reduced uncertainty. Increasing the accuracy of force estimates of other well studied CMEs will allow for a more complete view of the magnitude of the forces influencing CME propagation and will allow model parameters to be more accurately constrained.

REFERENCES

Antiochos, S. K., DeVore, C. R., & Klimchuk, J. A. 1999, ApJ, 510, 485

Aschwanden, M. J., Nitta, N. V., Wuelser, J.-P., Lemen, J. R., Sandman, A., Vourlidas, A., & Colaninno, R. C. 2009, ApJ, 706, 376

Bein, B. M., Berkebile-Stoiser, S., Veronig, A. M., Temmer, M., Muhr, N., Kienreich, I., Utz, D., & Vršnak, B. 2011, ApJ, 738, 191

Billings, D. E. 1966, A guide to the solar corona, ed. Billings, D. E.

Brueckner, G. E., et al. 1995, Sol. Phys., 162, 357

Byrne, J. P., Maloney, S. A., McAteer, R. T. J., Refojo, J. M., & Gallagher, P. T. 2010, Nature Communications, 1

Chen, J. 1996, J. Geophys. Res., 1012, 27499

Chen, J., Marqué, C., Vourlidas, A., Krall, J., & Schuck, P. W. 2006, ApJ, 649, 452

Colaninno, R. C., & Vourlidas, A. 2009, ApJ, 698, 852

Domingo, V., Fleck, B., & Poland, A. I. 1995, Sol. Phys., 162, 1

Emslie, A. G., et al. 2004, Journal of Geophysical Research (Space Physics), 109, A10104

Forbes, T. G., & Isenberg, P. A. 1991, ApJ, 373, 294

Forbes, T. G., & Priest, E. R. 1995, ApJ, 446, 377

Gallagher, P. T., Lawrence, G. R., & Dennis, B. R. 2003, ApJ, 588, L53

Howard, R. A., et al. 2008, Space Sci. Rev., 136, 67

Howard, T. A., Fry, C. D., Johnston, J. C., & Webb, D. F. 2007, ApJ, 667, 610

Howard, T. A., & Tappin, S. J. 2009, Space Sci. Rev., 147, 31

Kaiser, M. L., Kucera, T. A., Davila, J. M., St. Cyr, O. C., Guhathakurta, M., & Christian, E. 2008, Space Sci. Rev., 136, 5

Kliem, B., & Török, T. 2006, Physical Review Letters, 96, 255002

Krall, J., & St. Cyr, O. C. 2006, ApJ, 652, 1740

Lin, C.-H., Gallagher, P. T., & Raftery, C. L. 2010, A&A, 516, A44

Lin, J., & Forbes, T. G. 2000, J. Geophys. Res., 105, 2375

Lynch, B. J., Antiochos, S. K., DeVore, C. R., Luhmann, J. G., & Zurbuchen, T. H. 2008, ApJ, 683, 1192

Maloney, S. A., & Gallagher, P. T. 2010, ApJ, 724, L127

Mann, G., Jansen, F., MacDowall, R. J., Kaiser, M. L., & Stone, R. G. 1999, A&A, 348, 614

Manoharan, P. K., & Kundu, M. R. 2003, ApJ, 592, 597

Minnaert, M. 1930, ZAp, 1, 209

Munro, R. H., Gosling, J. T., Hildner, E., MacQueen, R. M., Poland, A. I., & Ross, C. L. 1979, Sol. Phys., 61, 201

Poland, A. I., Howard, R. A., Koomen, M. J., Michels, D. J., & Sheeley, Jr., N. R. 1981, Sol. Phys., 69, 169

Schrijver, C. J., Elmore, C., Kliem, B., Török, T., & Title, A. M. 2008, ApJ, 674, 586

van de Hulst, H. C. 1950, Bull. Astron. Inst. Netherlands, 11, 135

Vourlidas, A., Buzasi, D., Howard, R. A., & Esfandiari, E. 2002, in ESA Special Publication, Vol. 506, Solar Variability: From Core to Outer Frontiers, ed. A. Wilson, 91–94

Vourlidas, A., Howard, R. A., Esfandiari, E., Patsourakos, S., Yashiro, S., & Michalek, G. 2010, ApJ, 722, 1522

Vourlidas, A., Subramanian, P., Dere, K. P., & Howard, R. A. 2000, ApJ, 534, 456

Vršnak, B. 2006, Advances in Space Research, 38, 431

Zhang, J., Dere, K. P., Howard, R. A., Kundu, M. R., & White, S. M. 2001, ApJ, 559, 452

Zhang, J., Dere, K. P., Howard, R. A., & Vourlidas, A. 2004, ApJ, 604, 420